Letter

Laser-induced topological phases in monolayer amorphous carbon

Arnob Kumar Ghosh,* Quentin Marsal,† and Annica M. Black-Schaffer‡
Department of Physics and Astronomy, Uppsala University, Box 516, 75120 Uppsala, Sweden

(Received 13 August 2025; revised 24 November 2025; accepted 17 February 2026; published 5 March 2026)

Driving nontopological materials out of equilibrium using time-periodic perturbations, such as circularly polarized laser light, is a compelling way to engineer topological phases. At the same time, topology has traditionally only been considered for crystalline materials. Here we propose an experimentally feasible way of driving monolayer amorphous carbon topological. We show that circularly polarized laser light induces both regular and anomalous edge modes at quasienergies 0 and $\pm\pi$, respectively. We also obtain a complete topological characterization using an energy- and space-resolved topological marker based on the spectral localizer. Additionally, by introducing atomic coordination defects in the amorphous carbon, we establish the importance of the local atomic coordination in topological amorphous materials. Our work establishes amorphous systems, including carbon, as a versatile and abundant playground to engineer topological phases.

DOI: 10.1103/tp7r-31dj

Introduction. The Haldane model describing the anomalous quantum Hall effect (AQHE) in a hexagonal lattice without requiring an external magnetic field has been a foundation for topological phases of matter [1–3]. However, realizing the Haldane model in a static solid-state system has been experimentally challenging [4]. Moreover, for the best advantage of topological properties, it is preferable to have systems where topology can be controlled using a simple external control knob.

Floquet engineering via a time-periodic modulation of the Hamiltonian is precisely a simple and efficient way of manipulating band topology in an otherwise topologically trivial material [5–16], resulting in topological edge states at zero and/or finite energy in the spectrum [5,9–12,14,17–19]. For example, the Haldane model and its AQHE have recently been experimentally indirectly observed in monolayer graphene driven by a circularly polarized laser [20,21]. Floquet topological phases have also been observed in other experimental setups, such as photonic systems [22,23], acoustic setups [24,25], and cold-atomic systems [26,27].

While taking into account the spatial symmetries of crystalline materials greatly simplifies the characterization of their topology [28–31], this should not overshadow the fact that those symmetries are not required, as a recent work has emphasized in amorphous materials [32]. Importantly, amorphous solids are both abundant in nature and can be obtained in a vast diversity of materials, thus drastically extending the possibilities for topological physics. While amorphous materials lack translation symmetry, they are still characterized by a well-defined local atomic environment [33], set by the chemistry of their atomic constituents. This local order is a key feature for topology [34–45] and amorphousness enhances the diversity of achievable local environments [46]. Experimental observations in mechanical [35], photonic [41,47,48], and condensed matter platforms [49,50] further confirm the role played by local order.

Being able to combine the precise control of topology offered by a laser drive with the enhanced freedom of atomic structures in amorphous materials would open the way to an abundance of material platforms hosting controllable topologically protected modes not restricted by crystallinity. In this work, we demonstrate that a circularly polarized laser induces topological phases in monolayer amorphous carbon, an amorphous version of graphene [51]. We find both regular and anomalous edge modes at quasienergies 0 and $\pm\pi$, respectively. To overcome the broken translation invariance and the periodicity of the energy spectrum, we characterize its topology based on the spectral localizer [52]. We also study substitutional defects [53–57] introducing fourfold-coordinated sites in otherwise threefold-coordinated

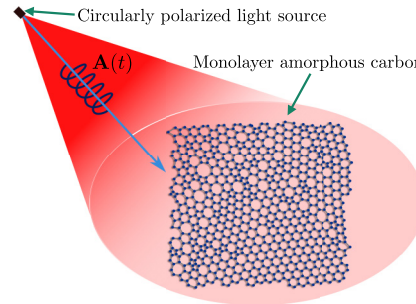


FIG. 1. Schematic representation of a circularly polarized laser beam with field $\mathbf{A}(t)$ on a monolayer amorphous carbon to engineer topological phases.

*Contact author: arnob.ghosh@physics.uu.se
†Contact author: quentin.marsal@physics.uu.se
‡Contact author: annica.black-schaffer@physics.uu.se

Published by the American Physical Society under the terms of the Creative Commons Attribution 4.0 International license. Further distribution of this work must maintain attribution to the author(s) and the published article's title, journal citation, and DOI. Funded by Bibsam.

monolayer amorphous carbon. We find topology to be robust to a moderate amount of such defects, but destroyed by a global change of the local atomic structure. This establishes local coordination as a key tool for topology in amorphous materials. Our results demonstrate that monolayer amorphous carbon becomes topological, despite lacking both the long-range order and bipartiteness of graphene, and highlight amorphous materials as versatile playgrounds for topological phases.

Material. We consider monolayer amorphous carbon [51], which can be experimentally obtained by electron beam irradiation of graphene [58]. This locally disorders the polygons formed by the carbon atoms, see lattice in Fig. 1, while crystalline graphene consists of only hexagons. Chemical vapor deposition at high temperatures has also been employed to create different polygons in otherwise monolayer graphene [51,59–61]. Due to the sp^2 hybridization of the carbon atoms, monolayer amorphous carbon remains exactly threefold coordinated [51] and, despite fluctuations resulting from geometric constraints, the average length d_0 of nearest-neighbor bonds is also similar to graphene. Such well-defined local properties are a key feature of amorphous materials [33]. In the last part, we additionally introduce coordination defects in the form of fourfold-coordinated sites. Such defects have been experimentally realized by bombarding graphene to create vacancies and substitutional transition metal or silicon sites [53–57].

The preserved local structure of monolayer amorphous carbon allows us to model the electronic properties using a spinless tight-binding Hamiltonian for the p_z orbital on each carbon atom with nearest-neighbor hopping amplitude t_h,

$$H = \sum_{\langle i,j \rangle} t_h^{ij} c_i^\dagger c_j + \text{H.c.}, \tag{1}$$

set on an amorphous lattice with exact threefold coordination, see Fig. 1. The lattice is obtained using a Voronoi tessellation of a random set of points following Ref. [40]. We incorporate the effect of varying bond lengths in the lattice through an exponential dependence of the hopping parameter, $t_h^{ij} = t_h \exp[-(|\mathbf{r}_j - \mathbf{r}_i| - d_0)/\lambda]$, where we set $t_h = 1$ as the energy unit, $d_0 = 1/\sqrt{3}$, and λ encodes the decay length of the hopping integral. We set $\lambda = \sqrt{3}d_0$, corresponding to the graphene second-nearest-neighbor distance, but our results do not depend on the choice of λ, as long as it remains of the order of d_0.

Drive. To induce topology in a monolayer amorphous carbon, we consider a driving protocol consisting of a circularly polarized laser, represented by a vector potential $\mathbf{A}(t) = A(\cos\Omega t, \sin\Omega t)$, where Ω is the frequency, $T = \frac{2\pi}{\Omega}$ its period, and A proportional to the light intensity. We consider the beam spot to be much larger than the system's dimension, such that there is no spatial variation in the light intensity, see Fig. 1. The circular polarization breaks time-reversal symmetry and is known to generate an energy gap in graphene, thereby allowing topological phases [10,18]. The driving field $\mathbf{A}(t)$ enters the Hamiltonian H in Eq. (1) through Peierls phase substitution in the electron hopping, such that $t_h^{ij} \to t_h \exp[-i\int_{\mathbf{r}_i}^{\mathbf{r}_j} \mathbf{A}(t)\cdot d\mathbf{r} - (|\mathbf{r}_j - \mathbf{r}_i| - d_0)/\lambda]$.

The time-periodic Hamiltonian $H(t) = H(t+T)$ can be treated using Floquet theory [12–16,62], allowing an effective time-independent description of the system. We compute the Floquet operator $U(T,0)$ from the time-dependent Hamiltonian in a time-ordered (TO) notation as $U(T,0) = \text{TO}\exp[-i\int_0^T dt H(t)]$. Numerically, we compute $U(T,0)$ by a Trotterization process as $U(T,0) = \prod_{j=0}^{N-1} U(t_j + \delta t, t_j)$, where $U(t_j + \delta t, t_j) = e^{-iH(t_j)\delta t}$, $\delta t = \frac{T}{N}$, and $t_j = j\delta t$, using 200 Trotter steps. The effective time-independent Floquet Hamiltonian is then computed as $H_F = -i\ln[U(T,0)]$, which captures the stroboscopic dynamics of the system and determines its spectral properties, including the local and total density of states (LDOS and TDOS). The spectrum of H_F is Ω periodic, such that the spectrum lies in the range $(-\Omega/2, \Omega/2]$ with $\pm\Omega/2 \equiv \pm\pi$. Thus, the driven system can host topological edge states at gaps at both 0 and $\pm\pi$ quasienergies [5,9–12,14,17–19].

Driven topological phases. We first demonstrate that the circularly polarized laser induces topological edge states through the spectral properties of driven monolayer amorphous carbon in Fig. 2. For this, we choose driving parameters such that the system hosts edge modes in both the 0 and π gaps (see orange star in Fig. 3). Before considering an amorphous system, we study (crystalline) graphene. We plot the quasienergy spectrum E_m as a function of the eigenvalue index m in Fig. 2(a) for driven graphene, with zoom-ins for the 0 and π gaps. We also compute the inverse participation ratio (IPR) of the eigenstates: $\text{IPR}(|\psi_m\rangle) = \sum_i |\langle i|\psi_m\rangle|^4$ and color code each eigenstate by its IPR. The IPR indicates localization by probing the inverse number of sites occupied by the state $|\psi_m\rangle$, ranging from 0 for a delocalized state in an infinite system, to 1 for a fully localized state. The IPR thus distinguishes between in-gap "localized" edge states (dark red) and bulk states (yellow to light red) in Fig. 2(a), with the color code also revealing the gap sizes. Next, we compute the LDOS for the states in the 0 and π gaps in Figs. 2(b) and 2(c), respectively. The LDOS shows that the gap states are localized along the edges, indicating topological origin. The presence of drive-induced topological modes in graphene is consistent with previous studies [10,18,20,63,64].

Next, we turn to monolayer amorphous carbon. Figure 2(d) and inset I1 surprisingly shows a drive-induced gap opening at $E = 0$, just as in graphene, with clearly localized in-gap states. The LDOS in Fig. 2(e) shows edge localization of this 0 mode. We also observe some localized states in the bulk, which are defect states appearing in amorphous systems and resulting in a finite bulk LDOS, also in the gap. For the π gap, the IPR reveals only a few localized states, indicating a gap closing at $\pm\pi$ compared to graphene, due to disorder-induced states. The LDOS for the π modes in Fig. 2(f) also does not exhibit a clear signature of the edge localization. Thus, the π modes are mostly unstable in monolayer amorphous carbon, most likely due to a smaller spectral gap protecting them from the bulk states. We also discuss this in terms of the stability of the topological invariant in Fig. 3. However, we can still find some parameters for which π modes are stable; see the Supplemental Material (SM) [65]. These results showcase that amorphous materials can be driven into topological phases, with associated edge modes. Notably, in terms of monolayer

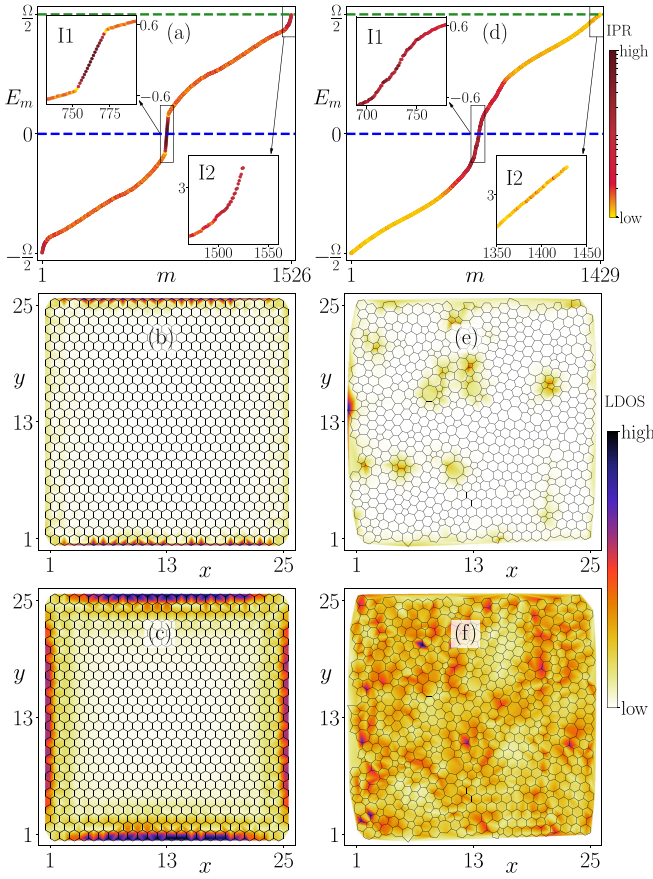


FIG. 2. (a) Quasienergy spectrum E_m as a function of eigenstate index m for crystalline graphene. Color encodes the IPR of the given state. Insets I1 and I2 show zoomed-in spectra close to $E = 0$ and π, respectively. (b), (c) Spatially resolved LDOS associated with states at quasienergy gaps 0 and π, respectively. (d)–(f) repeats (a)–(c) but for monolayer amorphous carbon. Here $A = 2.5$, $\Omega = 2.0$. For LDOS computation, we use a quasienergy window of $[-0.3, 0.3]$ in the 0 gap and $[\pm\Omega/2, \mp 0.1]$ in the π gap. Number of atoms in (a)–(c) is 1526 and in (d)–(f) is 1442.

amorphous carbon, this is despite losing both the long-range order and bipartiteness of crystalline graphene.

Topological characterization. Having established the existence of edge states, we provide a complete topological characterization of the system. This is challenging since monolayer amorphous carbon layer breaks translational symmetry and the driven system hosts modes at 0 and π quasienergies. Thus, we need both a real-space and energy-resolved topological invariant to fully characterize the system [52,66,67]. For this, we utilize the spectral localizer to obtain a space- and energy-resolved topological index [52,68–70]. The spectral localizer operator includes the system's position operators X and Y in the x and y directions, respectively, and the Hamiltonian, which for a driven system is taken as the effective Floquet Hamiltonian H_F [52]. Explicitly, the spectral localizer is defined as [52,68–70]

$$L_{x,y,E}(X, Y, H_F) = \kappa[(X - xI)\tau_x + (Y - yI)\tau_y] + (H_F - EI)\tau_z. \tag{2}$$

Here x, y, and E define the positions and energy where the spectral localizer is computed, κ ensures a compatible weight between the position operators and the Hamiltonian, and the Pauli matrices $\boldsymbol{\tau}$ satisfies the anticommutation relation $\{\tau_i, \tau_j\} = 2\delta_{i,j}$, forming the Clifford representation. We use $\kappa = 0.01$, which ensures stable evaluation. Utilizing $L_{x,y,E}(X, Y, H_F)$, the topological index, or Chern number, is defined as [52,68]

$$C_{x,y,E} = \tfrac{1}{2}\mathrm{sig}[L_{x,y,E}(X, Y, H_F)], \tag{3}$$

where sig is the signature of a matrix, counting the difference between the number of positive and negative eigenvalues. The numerical computation of the Chern number is made more efficient using LDLT decomposition; see the SM [65]. The topological index $C_{x,y,E}$ is both space and energy resolved and counts the number of boundary modes that cross through E; it is 0 outside of the system and takes a uniform finite value in the bulk; see the SM [65] for plots of $C_{x,y,E}$ in real space. To extract the topological invariant for the whole system, we compute $C_{x,y,E}$ at $E = 0, \pi$ for each site within a central region in the bulk and construct their average $C_{0,\pi}$. We further generate many different amorphous configurations and denote the final averages over all configurations as $\bar{C}_{0,\pi}$. We also compute the variance of the Chern numbers $C_{0,\pi}$ in real space, which indicates the stability of the Chern numbers. Another quantity from the spectral localizer is the localizer gap, which we define in the SM [65].

Figure 3 shows $\bar{C}_{0,\pi}$ in the A-Ω plane. First, we focus on crystalline graphene in Figs. 3(a) and 3(b). Regions with nonzero $\bar{C}_{0,\pi}$ denote topologically nontrivial graphene regions, generated by the circularly polarized laser. The phase diagram of irradiated pristine graphene has been studied before [11,63]. For high frequencies ($\Omega \gg$ bandwidth), we observe nonvanishing $\bar{C}_0 = -1$ while $\bar{C}_\pi$ remains zero, indicating that the system only supports topological modes at quasienergy 0. This can be understood as follows. In the high-frequency limit, the Floquet side bands, which are copies of the bands of the undriven system in frequency space, are far apart and thus overlap or direct transitions between them are forbidden [13,14,63]. However, virtual transitions between different Floquet side bands may still occur, which can modify the band topology of the system. Thus, in the high-frequency limit, one can obtain an effective Hamiltonian of driven graphene employing perturbation theory, which has been shown to effectively resemble the Haldane model [13,63]. If we now instead focus on lower to moderate frequencies ($\Omega \simeq$ bandwidth), the phase diagrams of both $\bar{C}_0$ and $\bar{C}_\pi$ consist of multiple nontrivial regions. At these lower frequencies, different Floquet side bands overlap and provide possibilities of band inversion occurring at both quasienergies 0 and $\pm\pi$ [5,9–12,14,16–19]. As a result, the driven system hosts topologically nontrivial edge states at both 0 and π quasienergies. For some parameters, we even observe higher Chern numbers, $|\bar{C}_{0,\pi}| > 1$.

Having discussed the generation of topological phases in crystalline graphene, we now showcase our main result, the phase diagrams for driven monolayer amorphous carbon in Figs. 3(c) and 3(d). Surprisingly, driven monolayer amorphous carbon closely resembles that of crystalline graphene. We only observe a slight reduction in the topological phases.

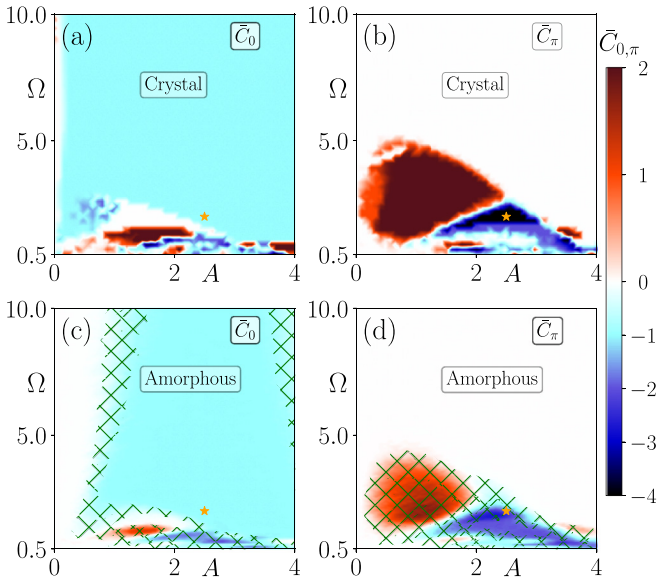


FIG. 3. Average Chern numbers (a) $\bar{C}_0$ and (b) $\bar{C}_\pi$ as a function of driving amplitude A and frequency Ω for crystalline graphene. Number of atoms in (a), (b) is 880. (c), (d) repeats (a), (b) for monolayer amorphous carbon. Green lines indicate regions with a finite variance of the Chern numbers. Orange star marks parameters used in Fig. 2. Averages of $C_{x,y,E}$ in each sample are calculated using a 7×7 square in the center of the system, and 30 different amorphous configurations are sampled with a system consisting of 837 atoms.

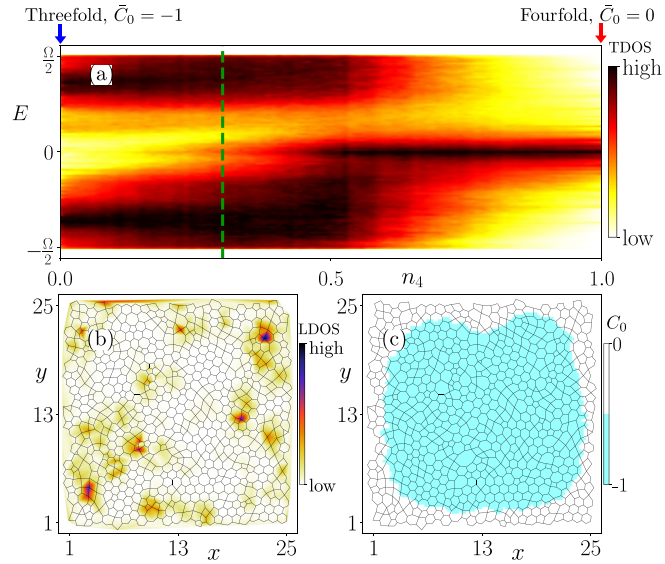


FIG. 4. (a) TDOS as a function of the fraction of fourfold-coordinated sites n_4 in driven monolayer amorphous carbon averaged over 50 random configurations of merging bonds, with all other parameters same as Fig. 2. Green line indicates the n_4 used in (b), (c). (b) LDOS and (c) Chern number C_0 for the 0 gap as a function of the system's dimension. For LDOS computation, we use a quasienergy window of [0.2,0.3] in the 0 gap.

We also shade the phase diagrams (green lines) where the spatial Chern number variance is nonzero, indicating a lack of stability of the corresponding phase. The variance reveals that the phase diagram for $\bar{C}_0$ is very stable apart from around the phase transitions between different Chern numbers. However, for $\bar{C}_\pi$ we find a finite variance in most of the phase diagram, implying that the π modes are not very stable, in agreement with the delocalized LDOS of the π modes, discussed in Fig. 2(f). Nevertheless, there still exists a small region where $\bar{C}_\pi \neq 0$ with vanishing variance, representing a stable π mode; see the SM for variance data [65]. Overall, the results demonstrate that monolayer amorphous carbon can easily host the regular 0, as well as anomalous π modes.

Local coordination. So far, we have focused on generating topology in driven monolayer amorphous carbon. Although monolayer amorphous carbon consists of polygons different from hexagons, all carbon atoms are still threefold coordinated. Next, we establish the importance of the local coordination, here threefold coordination, to generate the nontrivial topology. To this end, we consider the addition of fourfold-coordinated defect sites in the threefold-coordinated lattice, experimentally generated by vacancies or entrapment of other atoms [53–57]. We numerically obtain these defects by merging two neighboring threefold-coordinated sites into one. Further, considering an additional orbital on the fourfold coordinated sites does not give rise to a topological phase. Starting from a perfectly threefold-coordinated amorphous lattice, we arbitrarily partition the graph into dimers of neighboring sites and merge a fraction n_4 of them chosen at random. Thus, $n_4 = 0$ for a completely threefold-coordinated lattice, as previously, and $n_4 = 1$ for a fully fourfold-coordinated lattice. For intermediate n_4 values, we average over many different configurations of merging bonds.

We start with the same lattice and driving parameters as in Figs. 2(d) and 2(e). We compute the TDOS and observe how it evolves as the fraction of fourfold-coordinated sites n_4 is increased in Fig. 4(a). Since the π modes are unstable in this system, we only focus on the topological modes appearing in the 0 gap. At $n_4 = 0$, the system has two bands (dark red) separated by a gap which supports gapless edge states, as seen by its finite TDOS (yellow). The system also carries a finite Chern number $\bar{C}_0 = -1$ (marked by blue arrow). At low but nonzero n_4, the band structure and thus the topology are not affected. In this regime, fourfold-coordinated sites just behave as local defects, to which topological properties are robust. As the number of fourfold-coordinated sites increases, we observe that the two bands merge into one, around $n_4 \simeq 0.5$. This corresponds to the point where the fourfold sites start clustering and cannot be considered as local defects anymore. Rather, the lattice is now a mixture of two different local environments, three and fourfold coordinated. As the gap closes, the system also necessarily becomes nontopological, without any edge states. Finally, at $n_4 = 1$, the system consists of fully fourfold-coordinated sites, and it mimics the TDOS of a single band topologically trivial metallic square lattice, with $\bar{C}_0 = 0$ (marked by red arrow). To display the interesting intermediate behavior, we focus on $n_4 = 0.3$ [green line in Fig. 4(a)] and show the LDOS computed near the 0 gap and the Chern number C_0 in real space in Figs. 4(b) and 4(c), respectively. The LDOS pattern reveals the existence of edge states, along with some defect states appearing at the fourfold-coordinated

sites. The Chern number C_0 also gives a clear signature of the nontrivial topology, with $C_0 = -1$ inside the system.

Figure 4 discovers a crucial feature of the threefold-coordinated lattice, as in monolayer amorphous carbon. To support a topologically protected edge state, a system must possess at least two bands, which emerge from the sublattice degree of freedom in a threefold-coordinated lattice. Remarkably, the topological gap survives in the amorphous lattice, despite the two sublattices clearly mixing and thus the bipartition being lost. This demonstrates that local coordination is crucial, but that long-range ordering is not necessary to obtain topological states. In contrast, fourfold-coordinated lattices host no natural sublattices and thus, only feature one energy band, independent of the system being crystalline or amorphous. Hence, no light-induced topological gap can be opened.

Conclusion. In this work, we utilize a circularly polarized laser to theoretically engineer topological phases in monolayer amorphous carbon, which completely lacks translational symmetry and is topologically trivial in the static limit. In the low-frequency regime, we find both regular 0 and anomalous π modes. We calculate the spectral properties of the driven system with its signature of the edge states and use the spectral localizer to extract an energy- and space-resolved topological invariant to obtain the full phase diagram. Finally, we uncover the crucial importance of local coordination, here the threefold coordination of the monolayer amorphous carbon layer, and establish that the topological phase is destroyed when fourfold-coordinated sites become dominant. This reliance on local coordination makes the topology of amorphous materials fundamentally different from that of disordered materials. An interesting future direction is the exploration of driven amorphous systems via signatures such as a quantized orbital magnetization density [67,71].

Experimentally, periodic lasers have already been used to observe topological and Floquet side bands in crystalline graphene [64] and in other materials [72,73]. Similar experimental setups can also generate and detect the topological edge modes in monolayer amorphous carbon. To support this, we estimate the experimental parameters for Fig. 3 in real units [15]. Approximating the carbon-carbon hopping amplitude to $t_h = 2.7$ eV, the photon energy $E = \hbar\Omega$ is in the range 1.35–27 eV to reach the topological phase, with the corresponding laser wavelength $\lambda = hc/E$ being 900 nm (infrared)–50 nm (ultraviolet). The peak electric field intensity $E_0 = \hbar\Omega A/ea$ is in the range 10^9–10^{11} Vm^{-1}, for an estimate of the neighboring carbon-carbon distance $a = 1.4$ Å. The resulting laser field intensity $I = \frac{1}{2}c\epsilon_0 E_0^2$ is then in the range 10^{12}–10^{16} Wcm^{-2}, where ϵ_0 is the vacuum permittivity, resulting in both appropriate laser wavelength and power. At the outset, we note that the damage threshold for crystalline graphene for 800 nm light is 3×10^{12} Wcm^{-2} [74]. We expect comparable damage thresholds for monolayer amorphous carbon as well. Therefore, intensities in the lower part of the estimated range approaching 10^{13} Wcm^{-2} under short-pulse excitation are likely to be experimentally more viable. Overall, our work paves the way for controllable topological phases in amorphous systems based on local environment engineering.

Acknowledgments. We acknowledge financial support from the Swedish Research Council (Vetenskapsrådet) Grant No. 2022-03963 and the European Research Council (ERC) under the European Union's Horizon 2020 research and innovation programme (ERC-2022-CoG, Grant Agreement No. 101087096). Part of the computations were enabled by resources provided by the National Academic Infrastructure for Supercomputing in Sweden (NAISS), partially funded by the Swedish Research Council through Grant Agreement No. 2022-06725. The Python package Kwant [75] has been employed to construct the lattice setups.

Data availability. The data that support the findings of this article are openly available [76].

[1] F. D. M. Haldane, Model for a quantum Hall effect without landau levels: Condensed-matter realization of the "parity anomaly", Phys. Rev. Lett. **61**, 2015 (1988).

[2] X.-L. Qi and S.-C. Zhang, Topological insulators and superconductors, Rev. Mod. Phys. **83**, 1057 (2011).

[3] B. A. Bernevig, *Topological Insulators and Topological Superconductors* (Princeton University Press, Princeton, 2013).

[4] C.-Z. Chang, C.-X. Liu, and A. H. MacDonald, *Colloquium*: Quantum anomalous Hall effect, Rev. Mod. Phys. **95**, 011002 (2023).

[5] T. Kitagawa, E. Berg, M. Rudner, and E. Demler, Topological characterization of periodically driven quantum systems, Phys. Rev. B **82**, 235114 (2010).

[6] T. Kitagawa, T. Oka, A. Brataas, L. Fu, and E. Demler, Transport properties of nonequilibrium systems under the application of light: Photoinduced quantum Hall insulators without Landau levels, Phys. Rev. B **84**, 235108 (2011).

[7] N. H. Lindner, G. Refael, and V. Galitski, Floquet topological insulator in semiconductor quantum wells, Nat. Phys. **7**, 490 (2011).

[8] Z. Gu, H. A. Fertig, D. P. Arovas, and A. Auerbach, Floquet spectrum and transport through an irradiated graphene ribbon, Phys. Rev. Lett. **107**, 216601 (2011).

[9] M. S. Rudner, N. H. Lindner, E. Berg, and M. Levin, Anomalous edge states and the bulk-edge correspondence for periodically driven two-dimensional systems, Phys. Rev. X **3**, 031005 (2013).

[10] G. Usaj, P. M. Perez-Piskunow, L. E. F. Foa Torres, and C. A. Balseiro, Irradiated graphene as a tunable Floquet topological insulator, Phys. Rev. B **90**, 115423 (2014).

[11] P. M. Perez-Piskunow, L. E. F. Foa Torres, and G. Usaj, Hierarchy of Floquet gaps and edge states for driven honeycomb lattices, Phys. Rev. A **91**, 043625 (2015).

[12] A. Eckardt, *Colloquium*: Atomic quantum gases in periodically driven optical lattices, Rev. Mod. Phys. **89**, 011004 (2017).

[13] T. Oka and S. Kitamura, Floquet engineering of quantum materials, Annu. Rev. Condens. Matter Phys. **10**, 387 (2019).

[14] M. Rudner and N. Lindner, Band structure engineering and nonequilibrium dynamics in Floquet topological insulators, Nat. Rev. Phys. **2**, 229 (2020).

[15] C. Bao, P. Tang, D. Sun, and S. Zhou, Light-induced emergent phenomena in 2D materials and topological materials, Nat. Rev. Phys. **4**, 33 (2022).

[16] A. K. Ghosh, T. Nag, and A. Saha, Generation of higher-order topological insulators using periodic driving, J. Phys.: Condens. Matter **36**, 093001 (2024).

[17] L. Jiang, T. Kitagawa, J. Alicea, A. R. Akhmerov, D. Pekker, G. Refael, J. I. Cirac, E. Demler, M. D. Lukin, and P. Zoller, Majorana fermions in equilibrium and in driven cold-atom quantum wires, Phys. Rev. Lett. **106**, 220402 (2011).

[18] P. M. Perez-Piskunow, G. Usaj, C. A. Balseiro, and L. E. F. F. Torres, Floquet chiral edge states in graphene, Phys. Rev. B **89**, 121401 (2014).

[19] S. Yao, Z. Yan, and Z. Wang, Topological invariants of Floquet systems: General formulation, special properties, and Floquet topological defects, Phys. Rev. B **96**, 195303 (2017).

[20] J. W. McIver, B. Schulte, F.-U. Stein, T. Matsuyama, G. Jotzu, G. Meier, and A. Cavalleri, Light-induced anomalous Hall effect in graphene, Nat. Phys. **16**, 38 (2020).

[21] D. M. B. Lesko, T. Weitz, S. Wittigschlager, W. Li, C. Heide, O. Neufeld, and P. Hommelhoff, Optical control of electrons in a Floquet topological insulator, arXiv:2407.17917.

[22] M. C. Rechtsman, J. M. Zeuner, Y. Plotnik, Y. Lumer, D. Podolsky, F. Dreisow, S. Nolte, M. Segev, and A. Szameit, Photonic Floquet topological insulators, Nature (London) **496**, 196 (2013).

[23] L. J. Maczewsky, J. M. Zeuner, S. Nolte, and A. Szameit, Observation of photonic anomalous Floquet topological insulators, Nat. Commun. **8**, 13756 (2017).

[24] Y.-G. Peng, C.-Z. Qin, D.-G. Zhao, Y.-X. Shen, X.-Y. Xu, M. Bao, H. Jia, and X.-F. Zhu, Experimental demonstration of anomalous Floquet topological insulator for sound, Nat. Commun. **7**, 13368 (2016).

[25] R. Fleury, A. B. Khanikaev, and A. Alu, Floquet topological insulators for sound, Nat. Commun. **7**, 11744 (2016).

[26] G. Jotzu, M. Messer, R. Desbuquois, M. Lebrat, T. Uehlinger, D. Greif, and T. Esslinger, Experimental realization of the topological Haldane model with ultracold fermions, Nature (London) **515**, 237 (2014).

[27] K. Wintersperger, C. Braun, F. N. Ünal, A. Eckardt, M. D. Liberto, N. Goldman, I. Bloch, and M. Aidelsburger, Realization of an anomalous Floquet topological system with ultracold atoms, Nat. Phys. **16**, 1058 (2020).

[28] L. Fu and C. L. Kane, Topological insulators with inversion symmetry, Phys. Rev. B **76**, 045302 (2007).

[29] H. C. Po, A. Vishwanath, and H. Watanabe, Symmetry-based indicators of band topology in the 230 space groups, Nat. Commun. **8**, 50 (2017).

[30] J. Kruthoff, J. de Boer, J. van Wezel, C. L. Kane, and R.-J. Slager, Topological classification of crystalline insulators through band structure combinatorics, Phys. Rev. X **7**, 041069 (2017).

[31] B. Bradlyn, L. Elcoro, J. Cano, M. G. Vergniory, Z. Wang, C. Felser, M. I. Aroyo, and B. A. Bernevig, Topological quantum chemistry, Nature (London) **547**, 298 (2017).

[32] P. Corbae, J. D. Hannukainen, Q. Marsal, D. Muñoz-Segovia, and A. G. Grushin, Amorphous topological matter: Theory and experiment, Europhys. Lett. **142**, 16001 (2023).

[33] R. Zallen, *The Physics of Amorphous Solids* (Wiley-VCH GmbH, Weinheim, Germany, 1998).

[34] A. Agarwala and V. B. Shenoy, Topological Insulators in Amorphous Systems, Phys. Rev. Lett. **118**, 236402 (2017).

[35] N. P. Mitchell, L. M. Nash, D. Hexner, A. M. Turner, and W. T. M. Irvine, Amorphous topological insulators constructed from random point sets, Nat. Phys. **14**, 380 (2018).

[36] K. Pöyhönen, I. Sahlberg, A. Weststrom, and T. Ojanen, Amorphous topological superconductivity in a Shiba glass, Nat. Commun. **9**, 2103 (2018).

[37] I. Sahlberg, A. Weststrom, K. Pöyhönen, and T. Ojanen, Topological phase transitions in glassy quantum matter, Phys. Rev. Res. **2**, 013053 (2020).

[38] Y.-B. Yang, T. Qin, D.-L. Deng, L.-M. Duan, and Y. Xu, Topological amorphous metals, Phys. Rev. Lett. **123**, 076401 (2019).

[39] M. Costa, G. R. Schleder, M. Buongiorno Nardelli, C. Lewenkopf, and A. Fazzio, Toward realistic amorphous topological insulators, Nano Lett. **19**, 8941 (2019).

[40] Q. Marsal, D. Varjas, and A. G. Grushin, Topological Weaire–Thorpe models of amorphous matter, Proc. Natl. Acad. Sci. USA **117**, 30260 (2020).

[41] P. Zhou, G.-G. Liu, X. Ren, Y. Yang, H. Xue, L. Bi, L. Deng, Y. Chong, and B. Zhang, Photonic amorphous topological insulator, Light Sci. Appl. **9**, 133 (2020).

[42] J.-H. Wang, Y.-B. Yang, N. Dai, and Y. Xu, Structural-disorder-induced second-order topological insulators in three dimensions, Phys. Rev. Lett. **126**, 206404 (2021).

[43] P. Corbae, F. Hellman, and S. M. Griffin, Structural disorder-driven topological phase transition in noncentrosymmetric BiTeI, Phys. Rev. B **103**, 214203 (2021).

[44] K. Li, J.-H. Wang, Y.-B. Yang, and Y. Xu, Symmetry-protected topological phases in a Rydberg glass, Phys. Rev. Lett. **127**, 263004 (2021).

[45] C. Wang, T. Cheng, Z. Liu, F. Liu, and H. Huang, Structural amorphization-induced topological order, Phys. Rev. Lett. **128**, 056401 (2022).

[46] M. Le Gallo and A. Sebastian, An overview of phase-change memory device physics, J. Phys. D **53**, 213002 (2020).

[47] G.-G. Liu, Y. Yang, X. Ren, H. Xue, X. Lin, Y.-H. Hu, H.-x. Sun, B. Peng, P. Zhou, Y. Chong, and B. Zhang, Topological Anderson insulator in disordered photonic crystals, Phys. Rev. Lett. **125**, 133603 (2020).

[48] Z. Jia, M. Seclì, A. Avdoshkin, W. Redjem, E. Dresselhaus, J. Moore, and B. Kanté, Disordered topological graphs enhancing nonlinear phenomena, Sci. Adv. **9**, eadf9330 (2023).

[49] P. Corbae, S. Ciocys, D. Varjas, E. Kennedy, S. Zeltmann, M. Molina-Ruiz, S. M. Griffin, C. Jozwiak, Z. Chen, L.-W. Wang, A. M. Minor, M. Scott, A. G. Grushin, A. Lanzara, and F. Hellman, Observation of spin-momentum locked surface states in amorphous Bi_2Se_3, Nat. Mater. **22**, 200 (2023).

[50] S. T. Ciocys, Q. Marsal, P. Corbae, D. Varjas, E. Kennedy, M. Scott, F. Hellman, A. G. Grushin, and A. Lanzara, Establishing coherent momentum-space electronic states in locally ordered materials, Nat. Commun. **15**, 8141 (2024).

[51] C.-T. Toh, H. Zhang, J. Lin, A. S. Mayorov, Y.-P. Wang, C. M. Orofeo, D. B. Ferry, H. Andersen, N. Kakenov, Z. Guo, I. H. Abidi, H. Sims, K. Suenaga, S. T. Pantelides, and B. Özyilmaz, Synthesis and properties of free-standing monolayer amorphous carbon, Nature (London) **577**, 199 (2020).

[52] A. K. Ghosh, R. Arouca, and A. M. Black-Schaffer, Local and energy-resolved topological invariants for Floquet systems, Phys. Rev. B **110**, 245306 (2024).

[53] A. V. Krasheninnikov, P. O. Lehtinen, A. S. Foster, P. Pyykkö, and R. M. Nieminen, Embedding transition-metal atoms in graphene: Structure, bonding, and magnetism, Phys. Rev. Lett. **102**, 126807 (2009).

[54] W. Zhou, M. D. Kapetanakis, M. P. Prange, S. T. Pantelides, S. J. Pennycook, and J.-C. Idrobo, Direct determination of the chemical bonding of individual impurities in graphene, Phys. Rev. Lett. **109**, 206803 (2012).

[55] H. Wang, Q. Wang, Y. Cheng, K. Li, Y. Yao, Q. Zhang, C. Dong, P. Wang, U. Schwingenschlögl, W. Yang, and X. X. Zhang, Doping monolayer graphene with single atom substitutions, Nano Lett. **12**, 141 (2012).

[56] Q. M. Ramasse, C. R. Seabourne, D.-M. Kepaptsoglou, R. Zan, U. Bangert, and A. J. Scott, Probing the bonding and electronic structure of single atom dopants in graphene with electron energy loss spectroscopy, Nano Lett. **13**, 4989 (2013).

[57] X. Yan, Y. Jia, and X. Yao, Defects on carbons for electrocatalytic oxygen reduction, Chem. Soc. Rev. **47**, 7628 (2018).

[58] J. Kotakoski, A. V. Krasheninnikov, U. Kaiser, and J. C. Meyer, From point defects in graphene to two-dimensional amorphous carbon, Phys. Rev. Lett. **106**, 105505 (2011).

[59] P. Y. Huang, C. S. Ruiz-Vargas, A. M. van der Zande, W. S. Whitney, M. P. Levendorf, J. W. Kevek, S. Garg, J. S. Alden, C. J. Hustedt, Y. Zhu, J. Park, P. L. McEuen, and D. A. Muller, Grains and grain boundaries in single-layer graphene atomic patchwork quilts, Nature (London) **469**, 389 (2011).

[60] K. Kim, Z. Lee, W. Regan, C. Kisielowski, M. F. Crommie, and A. Zettl, Grain boundary mapping in polycrystalline graphene, ACS Nano **5**, 2142 (2011).

[61] O. V. Yazyev and Y. P. Chen, Polycrystalline graphene and other two-dimensional materials, Nat. Nanotechnol. **9**, 755 (2014).

[62] G. Floquet, Sur les équations différentielles linéaires à coefficients périodiques, Ann. Ecole Norm. Superieure **12**, 47 (1883).

[63] T. Mikami, S. Kitamura, K. Yasuda, N. Tsuji, T. Oka, and H. Aoki, Brillouin-Wigner theory for high-frequency expansion in periodically driven systems: Application to Floquet topological insulators, Phys. Rev. B **93**, 144307 (2016).

[64] M. Merboldt, M. Schüler, D. Schmitt, J. P. Bange, W. Bennecke, K. Gadge, K. Pierz, H. W. Schumacher, D. Momeni, D. Steil, S. R. Manmana, M. A. Sentef, M. Reutzel, and S. Mathias, Observation of Floquet states in graphene, Nat. Phys. **21**, 1093 (2025).

[65] See Supplemental Material at http://link.aps.org/supplemental/10.1103/tp7r-31dj for details of the topological invariant: LDLT decomposition, analysis of localizer gap, spatially resolved localizer gap and topological invariant, stable π mode, and variance of the topological invariant, which includes Refs. [77–79].

[66] P. Titum, E. Berg, M. S. Rudner, G. Refael, and N. H. Lindner, Anomalous Floquet-Anderson insulator as a nonadiabatic quantized charge pump, Phys. Rev. X **6**, 021013 (2016).

[67] L. P. Gavensky, G. Usaj, and N. Goldman, Středa formula for floquet systems: Topological invariants and quantized anomalies from Cesàro summation, Phys. Rev. X **15**, 031067 (2025).

[68] T. A. Loring, K-theory and pseudospectra for topological insulators, Ann. Phys. **356**, 383 (2015).

[69] T. A. Loring and H. Schulz-Baldes, Finite volume calculation of K-theory invariants, New York J. Math. **23**, 1111 (2017).

[70] T. A. Loring, A guide to the Bott index and localizer index, arXiv:1907.11791.

[71] F. Nathan, M. S. Rudner, N. H. Lindner, E. Berg, and G. Refael, Quantized magnetization density in periodically driven systems, Phys. Rev. Lett. **119**, 186801 (2017).

[72] Y. H. Wang, H. Steinberg, P. Jarillo-Herrero, and N. Gedik, Observation of Floquet-Bloch states on the surface of a topological insulator, Science **342**, 453 (2013).

[73] S. Zhou, C. Bao, B. Fan, H. Zhou, Q. Gao, H. Zhong, T. Lin, H. Liu, P. Yu, P. Tang, S. Meng, W. Duan, and S. Zhou, Pseudospin-selective Floquet band engineering in black phosphorus, Nature (London) **614**, 75 (2023).

[74] A. Roberts, D. Cormode, C. Reynolds, T. Newhouse-Illige, B. J. LeRoy, and A. S. Sandhu, Response of graphene to femtosecond high-intensity laser irradiation, Appl. Phys. Lett. **99**, 051912 (2011).

[75] C. W. Groth, M. Wimmer, A. R. Akhmerov, and X. Waintal, Kwant: A software package for quantum transport, New J. Phys. **16**, 063065 (2014).

[76] A. K. Ghosh, Q. Marsal, and A. Black-Schaffer, Laser-induced topological phases in monolayer amorphous carbon (Version v1) [Data set], Zenodo (2026), https://doi.org/10.5281/zenodo.18412848.

[77] N. Chadha, A. G. Moghaddam, J. van den Brink, and C. Fulga, Real-space topological localizer index to fully characterize the dislocation skin effect, Phys. Rev. B **109**, 035425 (2024).

[78] M. Bueno, S. Furtado, and C. Johnson, Congruence of Hermitian matrices by Hermitian matrices, Linear Algebra Appl. **425**, 63 (2007).

[79] A. Cerjan, T. A. Loring, and F. Vides, Quadratic pseudospectrum for identifying localized states, J. Math. Phys. **64**, 023501 (2023).